Microfluidic-Induced Growth and Shape-Up of Three-Dimensional Extended Arrays of Densely Packed Nanoparticles

Julie Angly,[†] Antonio Iazzolino,[†] Jean-Baptiste Salmon,[†] Jacques Leng,[†,*]
Sivasankaran Prathap Chandran,[‡,¶] Virginie Ponsinet,[‡] Anthony Désert,[§] Aurélie Le Beulze,[§]
Stéphane Mornet,[§] Mona Tréguer-Delapierre,[§] and Miguel A. Correa-Duarte[⊥]

[†]Laboratoire du Futur, Université de Bordeaux, UMR 5258, F-33600 Pessac, France, CNRS, Laboratoire du Futur, UMR 5258, F-33600 Pessac, France, and RHODIA, Laboratoire du Futur, UMR 5258, F-33600 Pessac, France, [‡]Centre de Recherche Paul-Pascal, Université de Bordeaux, UPR 8641, F-33600 Pessac, France, and CNRS, Centre de Recherche Paul-Pascal, UPR 8641, F-33600 Pessac, France, [¶]Department of Chemistry, Sri Sathya Sai Institute of Higher Learning, Prasanthi Nilayam Campus, Puttaparthi, Anantapur district, Andhra Pradesh - 515134, India, [§]Institut de Chimie de la Matière Condensée, Université de Bordeaux, UPR 9048, F-33600 Pessac, France, and CNRS, Institut de Chimie de la Matière Condensée, UPR 9048, F-33600 Pessac, France, and [⊥]Departamento de Quimica Fisica, Universidad de Vigo, 36310 Vigo, Spain

ABSTRACT We use evaporation within a microfluidic device to extract the solvent of a (possibly very dilute) dispersion of nanoparticles and concentrate the dispersion until a solid made of densely packed nanoparticles grows and totally invades the microfluidic geometry. The growth process can be rationalized as an interplay between evaporation-induced flow and kinetic and thermodynamic coefficients which are system-dependent; this yields limitations to the growth process illustrated here on two main cases: evaporation- and transport-limited growth. Importantly, we also quantify how colloidal stability may hinder the growth and show that care must be taken as to the composition of the initial dispersion, especially regarding traces of ionic species that can destabilize the suspension upon concentration. We define a stability chart, which, when fulfilled, permits us to grow and shape-up solids, including superlattices and extended and thick arrays of nanoparticles made of unary and binary dispersions, composites, and heterojunctions between distinct types of nanoparticles. In all cases, the geometry of the final solid is imparted by that of the microfluidic device.

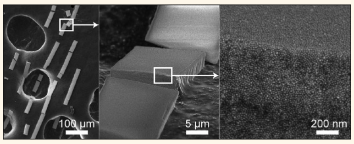

KEYWORDS: densley packed nanoparticles · microfluidic-induced growth · extended arrays

Clusters, crystals, or extended arrays of nanoparticles (NPs) display promising properties which, upon integration into devices, will promote the development of new technologies[1] and already pave the way to new paradigms.[2,3] Among many possible structures, crystals of nanocrystals (superlattices, SLs) are currently attracting an ever increasing research effort. SLs can be solution-processed, which is a key point for industrial up-scaling. They display crystalline structures which overcome by far their atomic analogues with, for instance, lattices that have no equivalent in nature.[4] Their existing or emerging properties range from magnetism, electronics, optics, energy conversion, catalysis, sensing, *etc.*[1,5−11] Eventually, they offer an important extension to the fundamental knowledge of colloidal science with new interactions between nano-objects, more morphologies, tunability, higher versatility, *etc.*

The main routes for SL fabrication fall into two categories: *equilibrium* and *out-of-equilibrium* processes, which are sometimes interwoven. The equilibrium route takes full advantage of thermodynamics applied to colloidal physical chemistry to nucleate SLs from bulk[6,12] or at an interface (liquid/solid or liquid/gas).[13,14] The classical interactions between colloids (electrostatics, steric, depletion, van der Waals) are enriched at nanoscale by a set of specific interactions such as facet-selective or reconfigurable ligands,[15−18] morphology-dependent forces,[19,20] size-tunable dipolar interactions,[21] and solvent-mediated interactions.[22] Astonishing crystalline morphologies have been obtained[23−25] with new structures and properties. In this fabrication route, the typical coherence length of the resultant material

* Address correspondence to jacques.leng-exterieur@solvay.com.

Received for review April 10, 2013 and accepted July 31, 2013.

10.1021/nn401764r

is rather modest—on the order of 1−100 μm—and due to the fabrication process, neither shaping-up nor integration seems straightforward.

The out-of-equilibrium routes nonexhaustively include sedimentation,[26] dielectrophoresis,[27] spin- or dip-coating,[28,29] and drying.[30] The latter method is by far the most often used for the fabrication of SLs[6] and is quite versatile, for example, drop casting, evaporation-induced self-assembly (EISA), evaporative coating, *etc.* Well known, quantified, and exploited at the microscale to engineer deposits or functional materials (sessile drop,[31] jet printing,[32] coatings,[33,34] EISA[35]), it basically relies on a local increase of the concentration upon solvent extraction to generate colloidal crystals and often takes advantage of capillary effects to guide microparticles. Transport phenomena, crucial in this matter, make the process rather complex: the flow induced by evaporation (including free-surface effects) transports the colloids, and both transport coefficients as well as evaporation itself may be concentration-dependent. The full process therefore results in an interplay between kinetics and thermodynamics. In the field of SLs, the drying-based driven assembly seems so far based on empirical and educated guesses[36] which nevertheless turn out extremely successful in terms of fabrication procedures.

Whatever their fabrication route, the integration of SLs in functional devices offers a promising prospect: the merging between microscaled *top-down* architectures and nanoscaled *bottom-up* assemblies.[37] Recent examples include the use of microfluidics to characterize[38] or optimize[39] the structure and growth of SLs, micromolding for the deposition of large and thick areas of SLs,[40] localization of SLs upon drying into patterned substrates,[41] transfer and nanoengineering of self-standing nanosheets,[42,43] *etc.*

Here we use *microevaporation*,[44−49] a microfluidic technique based on evaporation, that permits us to *grow and shape-up* extended, three-dimensional thick lattices of densely packed NPs (typical size of the final material 10 μm × 50 μm × 1 cm) with a fine control as to the positioning and composition of the array. The technique takes advantage of the selective permeability of an integrated membrane to extract the solvent of a dispersion but *not* the NPs. The latter get accumulated in a microchannel whose geometry is neatly defined by lithographic techniques, and upon sufficient accumulation, a dense state grows to eventually totally fill the channel (Figure 1). Importantly, the present microfluidic approach is fairly general and does not rely on a specific type of NPs, as long as they feature sufficient colloidal stability as we shall see latter, and actually works for a large set of solutes, from molecules to large colloids.

Microevaporation shares similarities with other evaporation-based techniques but has also its own spectrum of specificities. It takes from EISA[35] the driving force of evaporation but *suppresses all capillary effects* and works for *all solutes* (*i.e.*, from molecules to large colloids). It takes from micromolding (MIMIC[50]) the capability of casting a shape thanks to a PDMS mold; however, unlike MIMIC, it works *continuously* with the molding capillary connected to a reservoir *and* the evaporation permanently driven across a membrane, actually one wall of the capillary. Hence, the final material is not just a concentrated lump of the initial liquid present in the mold but can be continuously grown with time. As detailed later in the text, this continuous aspect of the process permitted us to fabricate a microscaled heterojunction between distinct arrays of NPs, which appears relevant in terms of device engineering.[51] More importantly, the tool is quite suitable to the quantification of the processes at work during the build-up of a solid at microscale. First, the evaporation is extremely well-controlled by design and imparts a definite pace to the concentration process. Then, *in situ* techniques such as Raman microimaging, on-chip small-angle X-ray scattering, optical microscopy and microspectroscopy, *etc.* help unveil the spatiotemporal features of the concentration dynamics and the coupled roles of concentration- and system-dependent evaporation and transport phenomena.

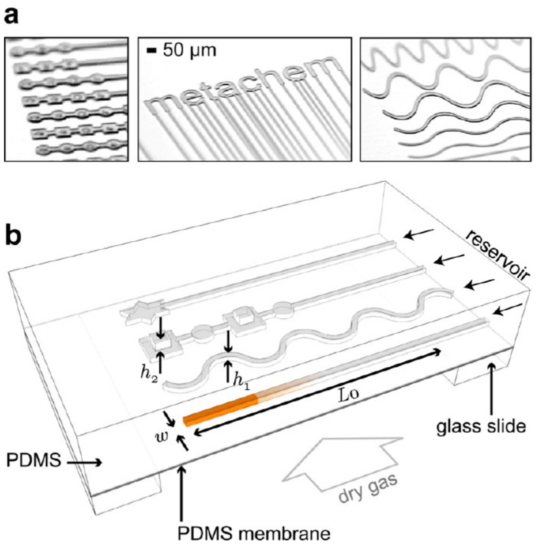

Figure 1. (a) Images of several resist-on-silicon patterns used for the fabrication of microfluidic devices. (b) Evaporation-based cell used for guided assembly of nanoparticles (NPs); evaporation proceeds across the thin PDMS membrane and induces a concentration mechanism that fills the channels with a solid made of densely packed NPs (orders of magnitude: $h_i \approx 5-20\ \mu$m, $w \approx 20-100\ \mu$m, $L_0 \approx 1-10$ mm; PDMS membrane thickness $e \approx 10-30\ \mu$m).

Here, we focus on aqueous dispersions of NPs and show how it is possible to grow solids owing a set of conditions regarding the stability of the dispersion; the latter must be very stable against precipitation in order to reach a compact state. Indeed, as dispersions of engineered NPs can be rather dilute to start with (volume fraction $\sim 10^{-6}$ to 10^{-4}, or about 10^{15} particles/L), any trace of pollutant may act as a precipitant upon concentration. On the basis of our specific process, we work out some general conditions that ensure the growth of a solid out of the dilute dispersion. In this framework, we evidence that the growth dynamics of the solid is chiefly governed by the physical chemistry of the dispersion (*e.g.*, the type of ligand on the NPs). All these results are assessed with simple theoretical arguments which yield a robust roadmap for growing micromaterials made of NPs. We illustrate the procedure with a series of solids—including SLs and composites—grown out of a variety of NPs with different shapes, chemistry, and functionality. Eventually, we take full advantage of the open-access reservoir of the microfluidic device to illustrate how to engineer heterojunctions and how to grow solids out of dispersions which are otherwise prone to precipitation.

RESULTS: CONTROL OF THE SOLID GROWTH

The device illustrated in Figure 1b works by extraction of the solvent from a channel in contact with a thin PDMS membrane ($\approx$10−30 μm). We focus here on the linear and planar geometry of Figure 1b, but the very same principle applies for all possible shapes of the channel. The latter can be nonplanar (*i.e.*, real 3D geometries) due to multilevel photolithography (Figure 1a). Due to the assumption of *local thermodynamic equilibrium*,[52] any concentration process can be rationalized on the basis of two coefficients, one of thermodynamic nature, the chemical activity a that expresses how the evaporation is altered by the presence of a solute, and one of kinetic nature, the collective diffusion coefficient D that describes the transport properties of the dispersion/solution. Using a basic scaling analysis of the concentration process given below, we design microevaporators which are capable of concentrating extremely dilute suspensions and grow and shape-up a solid of NPs in a controlled manner in a matter of hours.

Concentration Mechanism. *Conservation Laws.* For linear geometries, the evaporation flow rate Q_e is a key parameter and it is measured using an *ad hoc* calibration ($Q_e = \mathcal{O}(1-100\ \text{nL/h})^{48}$); for convenience, we introduce the lineic evaporation rate $q_e = Q_e/L_0$. The extracted solvent is replaced by a compensation flux coming from the reservoir, and this is the very basic mechanism which drives the solute from the reservoir toward the tip of the evaporation channel (as in suction pumps in plants[53,54]), where it accumulates. Such an evaporation-driven flux is induced by the difference of water chemical activity (or potential) across the membrane $a(\phi) - h_e$, where $a(\phi)$ is the concentration-dependent activity of water in the dispersion at solute volume fraction ϕ and h_e the humidity of the gas blown on the other side of the membrane (Figure 1b). This driving force induces permeation which translates into a local velocity $v(x)$ as expressed directly through the following local conservation equation:

$$hw\partial_x v = -(a(\phi) - h_e)q_e \qquad (1)$$

where h and w are the transverse dimensions of the channel (Figure 1) and L_0 is the evaporation length of the channel exposed to the membrane. In the rest, we make sure that $h_e = 0$ in all cases. In eq 1, $v(x)$ is the width- and height-averaged volume velocity in the channel,[52] x the long axis of the channel. Global mass conservation ensures that all the solvent that evaporates is replenished by a flux that comes in from the reservoir at a flow rate $Q_0 = V_0wh = q_eL_0$. Therefore, the natural scale for the velocity follows $V_0 = q_eL_0/wh$, where the evaporation time $\tau_e = wh/q_e$ emerges. It is the natural time scale of the process and corresponds to the time needed to empty one volume of channel. We notice here a benefit of miniaturization with the factor L_0/wh which amplifies the surface effect of evaporation and makes V_0 significant essentially because surface-to-volume effects are majored in these micrometer-sized devices. When pure water evaporates ($a = 1$), the evaporation-induced velocity profile simply reads $v(x) = -x/\tau_e$. Note that the above-mentioned conservation arguments simplify considerably in the geometrical limit of very flat channels ($h \ll w$) in contact with an ultrathin membrane ($e \ll w$) for which evaporation proceeds *across the membrane only*; therefore, $q_e = wv_e$, with v_e the evaporation velocity of water solubilized in the membrane well-described using a Fickean approach.

The induced flow drives solutes toward the tip of the microchannel and traps them only if the induced velocity dominates diffusion over the length of the channel L_0, as expressed by the Péclet number: $Pe = L_0V_0/D$. The solute—which does not evaporate—is conserved in the channel, and the kinetics of the concentration process $\phi(x,t)$ results from a convection−diffusion competition:

$$\partial_t\phi = -\partial_x[\phi v - D(\phi)\partial_x\phi] \qquad (2)$$

where $D(\phi)$ is the *collective diffusion coefficient*, a transport coefficient that describes how the solution/dispersion relaxes concentration gradients. In colloidal science, $D(\phi)$ is generally expressed as an interplay between osmotic compressibility and viscous drag in a dispersion.[55] Refs 48 and 49 give a detailed and practical use of these quantities in the present case of microfluidic evaporation.

Orders of Magnitude and Scaling Analysis. It is worth stressing again the benefits of the microfluidic format in the context of dispersions of NPs. Due to the neat control of the geometrical design and operation parameters, all physical scales of the process are precisely known: the thickness of the PDMS membrane and the dimensions of the channel altogether define the evaporation time τ_e (=10^2−10^3 s typically); the length L_0 of the channel and the evaporation time τ_e define the evaporation-induced velocity everywhere and, in particular, the entrance velocity $V_0 = L_0/\tau_e$.

Additionally, the knowledge of two coefficients $a(\phi)$ and $D(\phi)$ permits us to predict the exact spatiotemporal kinetics of the concentration process. In the case of ideal solutions [$a \equiv 1$ and $D \equiv D_0 = kT/6\pi\eta R$ from Stokes–Einstein relation, $D_0 = \mathcal{O}(10^{-12}\text{–}10^{-11}\ \mathrm{m^2/s})$ for NPs], the competition between convection and diffusion defines a length $p = (D_0\tau_e)^{1/2}$, which delineates the convection-dominated zone ($x > p$) and the diffusion-dominated zone ($x < p$). The concentration process is efficient only if $p < L_0$, that is, for a Péclet number $Pe = L_0V_0/D_0 = (L_0/p)^2 > 1$. For suspended nano-objects, $p \sim 100$ μm, which sets the minimal size of evaporators to be efficient.

For $Pe \gg 1$, the scaling analysis of the transport eq 2 shows that the diffusion-dominated region is permanently fed with NPs with an incoming flux ϕ_0V_0 with ϕ_0 the volume fraction of NPs in the reservoir, leading to a local ($x < p$) increase of the concentration: $\Delta\phi/\Delta t \sim \phi_0L_0/p\tau_e$. Working with extremely dilute suspensions therefore imposes strong constraints as to the design of our microevaporator; we indeed require the time Δt to concentrate a dilute suspension ($\phi_0 = 10^{-6}\text{–}10^{-4}$) into a dense state ($\phi_d \approx 0.5$) to be reasonable, that is, as most of order of hours. As $\Delta t \sim (\tau_e/\phi_0)(p/L_0)$, we design the device in order to maximize the length L_0 (up to centimeters) while scaling down the product $\tau_e p \sim \tau_e^{3/2}$, which we achieve by making very thin devices ($\tau_e \sim h/\nu_e$), which evaporate very efficiently (high ν_e) due to very thin membranes ($\nu_e \sim 1/e$). Evaporation is further sped up for small channel width w and well-separated channels.[53] Typical values are $e \approx 10$ μm and $h \approx 5$ μm (these are the values we use for the rest of this work), leading to $\tau_e \approx 50$ s. The latter value is actually obtained within % with a dedicated calibration method described previously.[48] It is worth mentioning that the scaling analysis strictly holds for dilute suspensions only, but in all cases we studied so far, it works well up to fairly concentrated regimes and thus remains a valuable tool for designing the evaporation devices.

Having designed, fabricated, and calibrated such evaporators, we can concentrate in a reasonable amount of time (order of hour) the initially dilute suspension until the nucleation and growth of a dense state occurs.

Transport- or Evaporation-Limited Growth. For $Pe \gg 1$, the NPs are trapped in the thin linear channel and get accumulated at its tip over time while permanently fed by a steady flux of solutes from the reservoir. Eventually, upon sufficient accumulation, nucleation of a dense state at $t = t_N$ may occur, followed by a growth kinetics. Figure 2a shows such a kinetics observed under a microscope and characterized using the (image-processed) position $x_d(t)$ of the front.

We display in Figure 2b,c two main limiting cases for the growth kinetics, which are actually fully tuned by the physical chemistry of the suspensions: *transport- and evaporation-limited growth*. Figure 2b shows the case of sterically stabilized NPs (Au@PEG, after the [core material]@[shell or corona material] nomenclature) for which the trajectory of the dense front slows down over time (whatever L_0, Figure 2b left); scaling the front with the respective lengths L_0 of the channels in which the fronts grow (Figure 2b right) and the time from nucleation with the natural evaporation time τ_e shows a good collapse which is well-described by a single exponential (solid black line). Inversely, the case of charge-stabilized NPs (Ag@SiO$_2$) shows a linear growth kinetics which also rescales well with the same dimensionless variables (Figure 2c right).

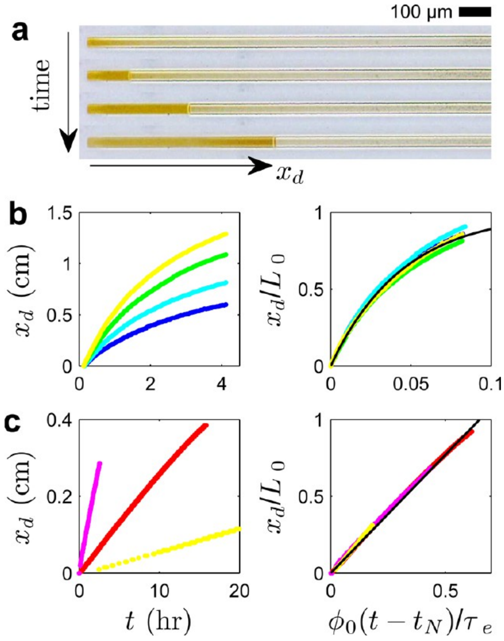

Figure 2. (a) Typical series of images acquired during the growth of a dense state made of NPs (here Ag@SiO$_2$). The temporal analysis of the growth kinetics leads to two limiting cases: (b) limited by the chemical activity yielding an exponential slowing down (Au@PEG in water with $\phi_0 = (3.3 \pm 0.1) \times 10^{-4}$ and $\tau_e = 56 \pm 2$ s, NPs with a core diameter ≈15 nm; one concentration ϕ_0 only and different L_0); (c) limited by the transport coefficient yielding a linear growth (Ag@SiO$_2$ in water with $\phi_0 = (2.3 \pm 0.3) \times 10^{-2}$ and $\tau_e = 480 \pm 20$ s; NPs with a silver core diameter of 20 nm and a silica shell 35 nm thick; one length L_0 only and different concentration ϕ_0).

We rationalize these results on the basis of a simple conservation law which balances the volume growth rate of the dense with the flux of incoming particles: $\phi_d\dot{x}_d \approx \phi_0\tilde{V}_0$, with $\tilde{V}_0$ specifying that the incoming flux is possibly altered by the presence of a dense state within the channel. Note also that we neglect here the concentration just before the front as it is very small in our present studies but may be significant in other cases.[48] Making dimensionless all the variables [with $X_d = x_d/L_0$, $T = (t - t_N)/\tau_e$, and $\Phi = \phi/\phi_0$], calling Φ^* the packing fraction of the growing solid, and introducing some specificity as to the physical chemistry of the system under study, we obtain two limiting cases for the growth rate:

•*Transport-limited growth* when the water evaporates as pure water independently of the colloid concentration: $\Phi^*\dot{X}_d \approx 1$; it holds whenever the water activity is barely altered by the presence of colloids such as, for instance, not-too-small silica-based colloids (with no grafted polymer), requiring actually a modest modification of the chemical potential of water with colloids. This modification scales like $\Delta\mu_w \sim k_BTv_s/v_c$, with k_BT the thermal energy, v_s the volume of the solvent molecules, and v_c that of colloids;[48] $\Delta\mu_w \ll k_BT$ even for small NPs. As a consequence, water evaporates as if it were pure, colloids get concentrated and pile-up into the dense state at a *constant rate* = $1/\Phi^*$; the growth actually stems from the diverging part of the osmotic compressibility of the diffusion coefficient $D(\phi)$ which prevents concentration gradients to be sustained: a dense state grows simply because it cannot be concentrated anymore. In such a case, there is always evaporation below the packed bed, a flow inside it, and *a flux of water into the solid* at the level of the front. In turn, the constant growth rate $1/\Phi^* = \phi_0/\phi_d$ justifies our choice to also include the initial concentration for rescaling the front position ($t \rightarrow \phi_0 t/\tau_e$): in this choice of units (Figure 2c right), the growth rate $\sim 1/\phi_d$ directly leads to the packing fraction of the dense state. Here, we find $\phi_d = 0.6 \pm 0.1$, which gives a first insight as to the structure of the dense state.

•*Evaporation-limited growth*, when, on the contrary, concentrated colloids modify significantly the water activity. It is the case of polymer-coated NPs where the polymer, here a PEG (Figure 2b left), dominates at very high concentration in lowering the water activity down to 0. In this case, we simply assume that water does not evaporate *at all* anymore above the dense state [$a = 0$ for $x < x_d$ and $a = 1$ otherwise], and the evaporation-induced velocity drops with the ever increasing dense state $\tilde{V}_0(x_d) = (L_0 - x_d)/\tau_e$ as a consequence of a diminished effective length of evaporation $L_0 \rightarrow L_0 - x_d$. This is the exponentially slowing-down mechanism of growth. Indeed, the growth kinetics reads $\Phi^*\dot{X}_d \approx 1 - X_d$, which admits an exponential solution $X_d = 1 - \exp(-T/\phi^*)$, fitting well our data, Figure 1b right. In this figure, ϕ_0 stands for the volume fraction of gold only (*i.e.*, the cores of the NPs), and we find $\phi_d \approx 0.10$. At this stage, the final composite is made of 10% gold NPs, the rest being (probably hydrated) polymer.

The nature of the growth kinetics, that is, linear or exponential, thus tells about the interplay between the way water evaporates in the dense state and how concentration gradients are sustained. We just saw two limiting cases where the growth is driven by (i) a diverging diffusion coefficient or (ii) stopped evaporation, but there are of course intermediate regimes between these two limiting cases. It is, for instance, the case of NPs strongly interacting *via* electrostatics[47] for which the basic conservation law must be modified to account for interaction-dependent transport coefficient or surfactant molecules[49] for which both the evaporation and the transport phenomena are mesophase-dependent. It remains that the knowledge of basic kinetic and thermodynamic data (a and D) permits us to predict the growth kinetics, and that its image-processed inspection (Figure 2) yields an estimate of the packing fraction in the dense phase.

Stability Issue. The previous scenarios hold only if no "accident" such as precipitation or aggregation occurs en route toward high concentration. The depiction of a binary system with NPs in water *only* is actually somewhat utopistic; we cannot elude the presence of pollutants solubilized in water which may play the role of destabilizing agent. Indeed, our evaporation-based device leads to an increase of the concentration of *all species*—although at different rates—and the localized increase of pollutant may well induce the aggregation of the dispersion. As we are working with extremely dilute dispersions of NPs, what matters is how much pollutant is present in the initial dispersion because even traces might play a significant role upon concentration.

For the sake of illustration, we consider here a specific case of traces of salt present in the dispersion of silica NPs in water. It could also be the case of solubilized PEG oligomers acting as depleting agents. We model the stability of the dispersion at the lowest level using a binary stability ratio W (the ratio of the aggregation rate at a given salt concentration to the one of an unstable dispersion[55]): $W \rightarrow \infty$ below a critical salt concentration c_s leading to a stable dispersion, and $W = 1$ above with near immediate aggregation. Then, assuming that in the dilute regime $a \equiv 1$ and $D \equiv$ const. (D_c for colloids and D_s for salt) in eqs 1 and 2, we solve the dynamics of the concentration process for both the colloids and the salt assuming they are independent, which is reasonable in the dilute regime only. In dimensionless variables, the control parameters are the salt concentration $C = c/c_0$ (c_0 is the salt concentration in the reservoir), the volume fraction of colloids $\Phi = \phi/\phi_0$ (ϕ_0 is the volume fraction of NPs in the reservoir), the Péclet number of salt Pe and that of colloids Pe_c. We gave elsewhere analytical solutions[46] for the full concentration process $C(X,T)$ and $\Phi(X,T)$ in the dilute regime, which we recall in the Supporting Information, and we examine here the issue of the coupled dynamics regarding the stability of the dispersion. We do not discriminate between heterogeneous (on the wall) or homogeneous aggregation (between particles) and just assume that the dispersion may become unstable above C_s. We identify two limiting cases for which there is either *precipitation only* or *growth only*. In brief (all details in the Supporting Information), if the concentration of salt in the reservoir

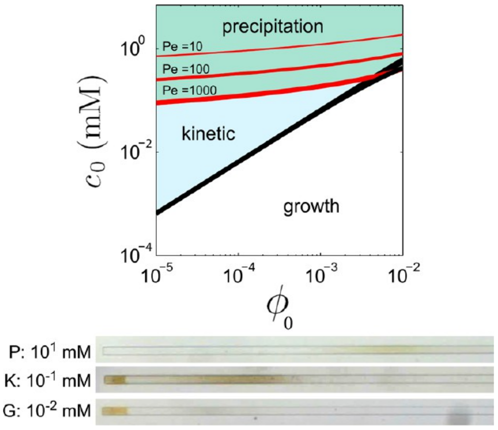

Figure 3. Top: stability chart giving the outcome of the concentration process (*growth* of a solid, *precipitation* of NPs, and mixed *kinetic* regime; see text) depending on the volume fraction ϕ_0 of NPs and the concentration c_0 of an electrolyte *in the reservoir* (or, equivalently, in the stock dispersion). The present chart is calculated for charge-stabilized NPs, which become unstable above a critical salt concentration; *Pe* in the figure stands for the Péclet number of the salt, the one of the NPs being considered nearly infinite (all details of the calculation are given in the Supporting Information). Bottom: examples of the three states described in the stability chart (P: precipitation, K: kinetic, G: growth), induced here with the amount of added salt (NaCl) indicated on the figure (and $\phi_0 = 2.3\%$); the width of the channel is 40 μm and pictures taken about 3 h after the beginning of the concentration process.

is too high, the salt concentration at the tip of the evaporator will overcome C_s before the NPs get sufficient time to nucleate a dense state (*precipitation regime*); conversely, when the concentration of salt is low enough in the reservoir, nucleation may occur and the growth will be fast enough to escape the region where the salt gets accumulated (*growth regime*).

We summarize these calculations on a stability chart (Figure 3) which delineates these two limiting cases as a function of the volume fraction ϕ_0 of the dispersion and the concentration of salt c_0 both taken *in the reservoir*, that is, in the native dispersion. We also evidence an intermediate regime (*kinetic regime*) in which the two kinetics are so close that interwoven events may occur such as precipitation followed by growth or even re-entrant transition as growth/precipitation/growth. All these states have been observed experimentally and are illustrated in Figure 3 where we concentrated a dispersion of Ag@SiO$_2$ NPs with a *controlled* amount of added salt.

Importantly, we find that the growth-only upper boundary does not depend on the Péclet number of colloids and reads $\Phi^* \ll C_s$ in dimensionless units, or with dimensions simply

$$\frac{c_0}{c_s} \ll \frac{\phi_0}{\phi_d} \tag{3}$$

where we recall that ϕ_d is the volume fraction of the dense state ($\mathcal{O}(1)$), ϕ_0 and c_0 the concentrations of NPs and salt in the reservoir, respectively, and c_s the concentration at which the dispersion becomes unstable ($c_s \approx 10-100$ mM for typical charge-stabilized systems). It thus permits us to rapidly estimate whether a dispersion can be grown into a dense state or will precipitate.

As a rule of thumb, we notice that charge-stabilized NPs are prone to aggregation especially when working at low concentration. For a typical sol–gel-processed silica coating on the NPs (*e.g.*, with a zeta-potential on the order of −40 mV at pH 5–7), traces of salt on the order of 1–10 μM are sufficient to prevent growth of a suspension with $\phi_0 \approx 10^{-6}-10^{-5}$. Increasing ϕ_0 by a factor of 10 to 100, by centrifugation for instance, is sufficient to escape the stability trap, and silica then becomes a very good stabilizer against aggregation for moderately diluted dispersions. We will discuss in the last section of this article another way of escaping the stability trap by the use of a microfilter.

Alternatively, sterically stabilized NPs with a grafted polymer are especially stable assuming there is no depleting agent in the dispersion (such as nongrafted polymers) that would be deleterious to the growth process. Here, we used several polymers but present mostly results concerning PEG-grafted NPs for which a thorough wash of the dispersion is required to eliminate unattached polymers and prevent depletion between NPs or between the particles and the wall of the microfluidic cell.

DISCUSSION: SHAPING BULK MATERIALS MADE OF NPS

Growing a material out of a dispersion of nano-objects thus requires colloidal stability. Assuming this or designing the NPs for this purpose, we demonstrate below that all sorts of dispersions can be assembled into dense, real 3D materials. A quantitative analysis of the structure on a specific case (15 nm diameter spherical Au@PEG NPs) using X-ray scattering shows that the particles crystallize into SLs, yet with small-size crystallites (≈μm). Experimentally, we also evidence that the order of these superlattices could be drastically improved with more calibrated dispersions. Anisotropic particles and mixtures of NPs can also readily be assembled thanks to microevaporation. Eventually, we show that heterostructures can be engineered by growing side-by-side materials made of different types of particles.

Structure. We start with Au@PEG and Au@SiO$_2$ NPs dispersed in water (same core, 15 nm diameter, spherical, and liganded with a 5 kDa PEG or capped with a 20 nm thick silica shell) which we concentrated until a dense state grew over several millimeters (Figure 2 and Figure 4a using an optimized chip with a thickness of 5 μm and a volume fraction of NPs larger than $\phi_0 = 10^{-4}$ in order to prevent precipitation in the case of Au@SiO$_2$ NPs). The growth kinetics of such a micromaterial is best quantified in the linear geometry of Figure 2;

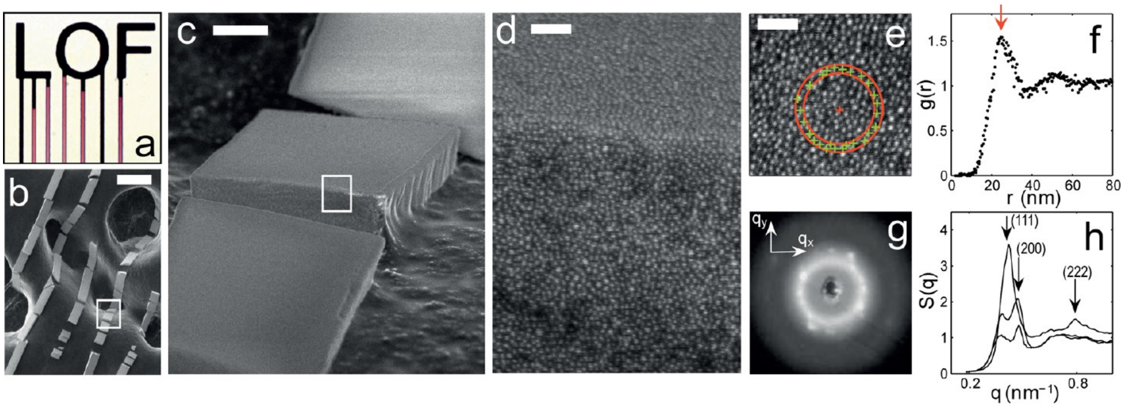

Figure 4. Images and structure of solids densely packed with NPs: (a–d) Au@SiO$_2$ with a 15 nm diameter core and a silica shell 20 nm thick, (e–h) Au@PEG with a 15 nm diameter core and a corona made of 5 kDa PEG grafted with thiols. (a) Tip of a tailor evaporation-based cell seen under a microscope and where the NP suspension undergoes a nucleation/growth kinetics (width of smallest channels 20 μm, height $\approx$ 5 μm). (b–d) Dense state resulting from (a) after drying and stamping onto a SEM substrate observed with SEM at several degrees of magnification (scale bar is 50 μm in b, 5 μm in c, and 150 nm in d). (e,f) SEM high magnification of the surface of the dense material (scale bar 100 nm) and pair correlation function *g*(*r*) calculated after particle centers registration. (g,h) *In situ* microfocused small-angle X-ray pattern and angular averaging of various patterns such as (g) yielding the structure factor *S*(*q*) *vs* wave vector *q* indexed in (h) for a fcc structure with lattice parameter of 28 nm, gold volume fraction of 0.27. The presence of Bragg peaks in the pattern of (g), also related to the marked peaks in the angular averagings presented in (h), demonstrates the local crystalline order of the NPs.

however, other geometries can be designed using soft lithography, including "device-oriented" shapes in which the growth takes place in the very same fashion (Figure 1 and Figure 4a).

We demonstrate that the micromaterial is made of densely packed NPs by monitoring its structure under a high-resolution scanning electron microscope (SEM). First, we peel off the membrane of the evaporation microfluidic chip and stamp the micromaterials onto a conductive tape previously stuck on a SEM substrate (a metallic pin). This transfer process is very efficient but somewhat brutal, and the structure sometimes breaks at places (Figure 4b); in this figure, we recognize the linear aspect of the micromaterial and we take advantage of the alveolar structure of the conductive tape to have some parts of micromaterial exposed to the electron beam with a slanted view. Zooming in such a zone (Figure 4c) evidences a brick-like edifice with neat facets and edges that actually reflect how the microfluidic channel promotes the shaping process. An even higher magnification (Figure 4d) now shows that the material is indeed made of tightly packed NPs, with here no obvious long-range order, and that the upper facet of the material is extremely smooth with a roughness basically set by the size of the NPs. The flatness of the material thus lies well within optical quality (here $\approx\lambda/20$), thanks to the PDMS molding; it is a crucial point for the optical characterization.

The volume fraction occupied by NPs in this composite is on order of 25%, the rest consisting of polymer, as consistently demonstrated using SEM image analysis and *in situ* X-ray scattering. From a SEM image acquired on the upper face of the material with its normal parallel to the electron beam, we construct the pair correlation function *g*(*r*). It is achieved by first registering the position of all particles (about 3000 on a typical image) and by then calculating the number of particles at a distance $r + dr$ from a given one (Figure 4e; the red circles and green crosses illustrate the counting procedure). The calculation is repeated for all distances and ensemble-averaged over all particles. The pair correlation function *g*(*r*) is normalized to 1 at high distances leading to the surface density of particles $\sigma = (1.37 \pm 0.06) \times 10^{15}$ particles/m^2. The correlation function exhibits an oscillating behavior with a modest peak at $r_m \approx 28$ nm (red arrow, Figure 4f), the mean distance between first neighbors. The shape of *g*(*r*) along with the height of the peak suggests that the planar organization of NPs is amorphous, with no long-range order.[56] The surface fraction occupied by the gold cores is $\phi = 4\pi\sigma r_p^2 = 0.25 \pm 0.06$.

Alternatively, we used small-angle X-ray scattering (SAXS) with a microfocused high brilliance beamline (spot diameter $\approx$1.5 μm, ID13, ESRF, Grenoble, France) to probe the structure of the micromaterial.[47] The latter was scanned pointwise directly into the chip, and diffraction patterns (Figure 4g) vary significantly from point to point but always exhibit Bragg spots superimposed to diffuse rings. From the measured form factor of the Au@PEG particles, we calculate the angular-averaged structure factor *S*(*q*) of the assembly as shown on Figure 4h for three different locations within the material. A basic analysis suggests that the structures we observe are compatible with face-centered cubic (fcc, indexing in Figure 4h) grains of a typical coherence length $\xi \sim \mu$m, seen under different orientations, with a NP packing fraction $\approx$0.27 and a lattice parameter of 28 nm, which compares well with the SEM image analysis. A refined analysis is made quite complex by the fact that the powder-averaging is actually poor due to the small coherence of the crystalline lattice ($\xi/r_m \approx 30$ where r_m is the distance between

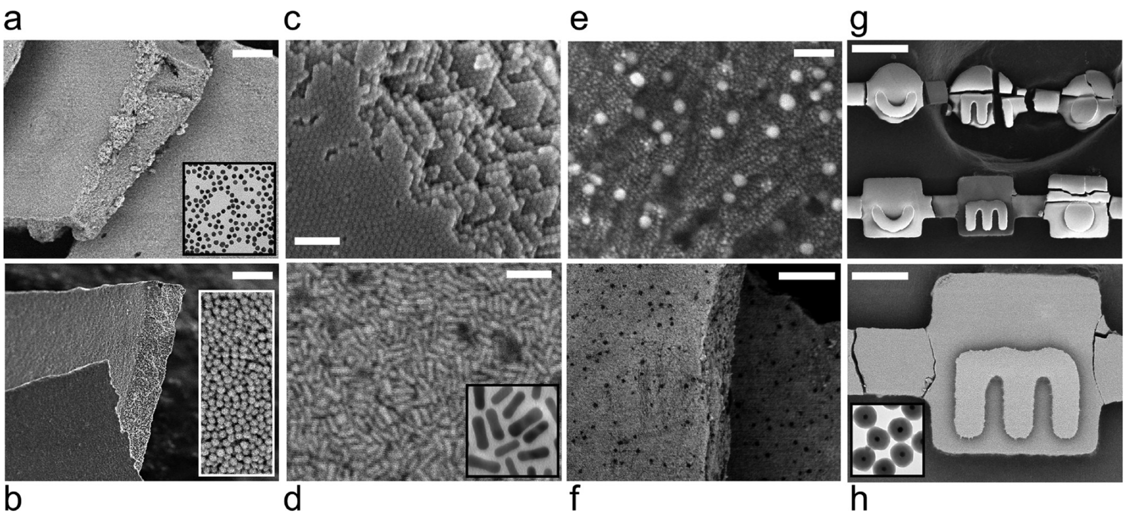

Figure 5. Catalog of dense structures generated with microevaporation and observed with a SEM: (a) Au@PEG 15 nm diameter (bar is 1 μm, inset is a TEM picture of native particles); (b) Au@PEG 60 nm diameter (bar is 1 μm, inset is a SEM picture of the surface of the material); (c) 80 nm diameter silica NPs (bar is 500 nm); (d) Au@PEG nanorods (bar is 100 nm, inset is a TEM picture of nanorods); (e) mixture of Au@PEG 15 and 60 nm (bar is 200 nm); (f) mixture of 15 nm Au@PEG and 80 nm silica NPs (bar is 1 μm); (g) Ag@SiO_2 NPs in 3D channels (bar is 50 μm); (h) same sample seen at higher magnification (bar is 10 μm, inset is a TEM view of native core−shell NPs).

first neighbors) and few grains only in the thickness of the cell ($h/\xi \approx 5$).[57,58] The presence of Bragg spots (Figure 4g) is however a definite proof of SLs, but with a limited spatial extent; it may be due either to the non-negligible size dispersity of the native gold NPs or to the rate at which the solid is built.[59] We leave open this question but nevertheless evidence below that, with very monodisperse NPs, long-range crystallization is obvious even from a SEM image.

Eventually, we notice that the volume fraction obtained from structural analysis (≈0.3) is higher than the one estimated directly by monitoring the growth rate of the solid (≈0.1) (while for other cases, such as large colloids, both analyses coincide[48]). We believe it comes from the fact that samples were dehydrated or left in a dry atmosphere before structural analysis.

From Simple Materials to Tailor Composites. We now turn to a description of a few structures we could build (Figure 5) and emphasize some of their features. First, we notice that the micromaterials we fabricate are very planar, basically *self-standing thick films*; depending on their type, they can be brittle and fragile but it is possible to extract millimeters of them out of the chip. Au@PEG materials are especially easy to grow (we achieved materials with 15 and 60 nm core diameter, Figure 5a,b) and mixtures thereof (Figure 5e) but exhibit little surface order, although we know from above that the surface inspection may hide the bulk organization. For comparison, commercial silica NPs (80 ± 5 nm diameter, polydispersity assessed from SAXS analysis) grow under obvious, hexagonal-like crystalline habits (Figure 5c).

Anisotropic particles assemble as well into close-packed assemblies, and we could grow dense materials of nanorods (Figure 5d), nanocubes, and nanodisks (not shown), all stabilized by polymers. In the present case of Au@PEG nanorods (long axis 37 ± 7 nm, small axis 11 ± 2 nm), it was somewhat expected[12] that these particles did not get oriented at all; it is indeed known that aligning such modest aspect ratio rods (≈2−3) rather requires a thermodynamic approach with a fine-tuning of the interaction parameters between the rods.[60−62]

Mixtures of small and large NPs readily assemble (Figure 5e,f), but some care must be taken as to the mutual interactions between small and large colloids. For instance, mixtures of Au@PEG small particles with larger SiO_2 NPs are unstable at high concentration for most of the mixture ratios we examined, probably due to hydrogen bonding between the PEG and the silica surfaces likely to generate aggregates en route toward high concentrations. We illustrate in Figure 6 a robust formulation for the fabrication of composite binary solids made of large SiO_2 NPs and small Au@SiO_2 NPs, here characterized by a ratio in number R (large-to-small). The final materials are quite homogeneous at the macroscopic level (Figure 6, top right) and absorb light in relation to the amount of gold inclusions (up to opaque samples for $R \to \infty$, *i.e.*, only small gold NPs) but appear somewhat heterogeneous at the nanoscale. Interestingly, for $R = 1.$ the large silica NPs crystallize at places but not everywhere (Figure 6, bottom left) and the disorganized zones seem correlated to a larger local amount of small inclusions. For higher ratios, it becomes possible to decorate the large NPs with a large number of small satellites (Figure 6, bottom right) and to reach structures with a connected network of plasmonic inclusions embedded in a dielectric substrate. These structures resemble much the ones manufactured with preassembled nanoclusters, such as in Figure 7, bottom right. The "binary" route hence turns

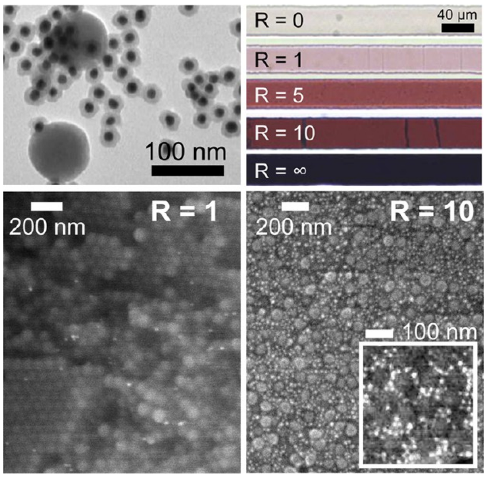

Figure 6. Top left: TEM picture of a binary mixture of large silica NPs (80 nm diameter) and small Au@SiO$_2$ NPs (15 nm core diameter, 10 nm thick silica shell). Top right: micromaterials obtained from binary dispersions with different ratio in number R of large-to-small particles. Bottom left: SEM pictures in backscattering mode for $R = 1$. Bottom right: SEM picture for $R = 10$, with the inset showing the same structure in backscattering mode.

out useful to simplify the fabrication process of advanced assemblies.

Eventually, we grew dense materials of core–shell Ag@SiO$_2$ NPs into 3D cavities (Figure 5g,h, silver core diameter 20 nm, silica shell thickness 35 nm) and the bottom-up-assembled final material nicely replicates the top-down-designed microfluidic chambers, with details fixed by the soft lithography technique used here (*i.e.*, order of μm). Here again, the structure of the colloidal assembly (detailed elsewhere[63]) is not ordered at long-range as probably limited by the size dispersity of core–shell Ag@SiO$_2$ NPs, and some faceting of the NPs is observed in the final solid.[63]

Active Control of Growth: Heterostructures. Heterostructures based on NPs can be built by taking advantage of a *sequential-filling approach*. Microevaporation chips can be engineered with a 50 μL open-access reservoir (Figure 7a) which permits us to tune *in time* the solution to be concentrated. By sequentially filling the reservoir with different dispersions, we accumulate different NPs and grow dense states in a sequential manner, which results in a layered material.

Figure 7a (right) also illustrates the corresponding protocol during which the reservoir is initially filled with pure water (W); at a given time, the water in the reservoir is replaced with dispersion or solution S_1 at concentration ϕ_0^1 which is left to concentrate for a lapse of time Δt_1; the dispersion is then replaced with pure water again. In linear geometries, solute conservation ensures that the particles driven inside the chip by evaporation contribute to build a linear dense state with a growth rate $\dot{L}_1$ (system-dependent, Figure 2). The total length of material $L_1 \approx \dot{L}_1 \Delta t_1$ is thus controllable by simply playing with the lapse of time Δt_1 and the concentration in the reservoir ϕ_0^1. Then, the reservoir is flushed with pure water, and after a delay time that permits the dense state to equilibrate, water is replaced by the second solution S_2 during Δt_2 and flushed again with water to build a second material of length L_2 next to the first one. The pipetting operation can be iterated as often as required and even automated with a liquid-handling robot to build tailor heterostructures.[48]

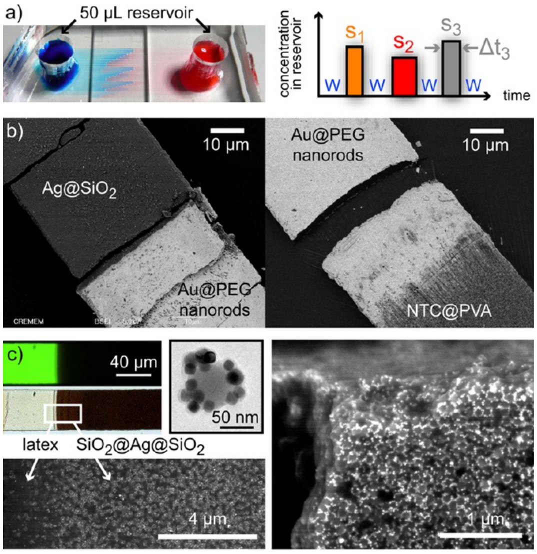

Figure 7. Protocol for building heterojunctions at the nanoliter scale. (a) The chip we use possesses a 50 μL open-access reservoir in which we can pipet sequentially several dispersions or solutions during a known lapse of time (top right for the pipetting workflow). It enables us to build a sequential solid, here illustrated with (b) a double junction made of Ag@SiO$_2$ next to Au@PEG nanorods next to carbon nanotubes CTN@PVA or (c) a simple junction between large latexes and engineered nanoraspberries SiO$_2$@Ag@SiO$_2$, the bed of latexes acting as a filter for salt; see text.

Figure 7b shows such a heterostructure obtained by sequential filling with Ag@SiO$_2$ followed by Au@PEG nanorods and then CNT@PVA (surfactant-stabilized carbon nanotubes mixed with a polymer, polyvinyl alcohol, in water). The respective lengths of different segments are on the order of millimeters, and we observe that the junction between the successive dense states extends on a length on the order of a few micrometers (1–10 μm) and depends on the nature of the materials that grew before. Beside the SEM images of Figure 7b, we also used a higher-energy electron beam to probe at the level of the junction the depth of the material (not shown) and the spatial extent of the composition gradient. It is quite obvious in Figure 7b that the Ag@SiO$_2$/Au@PEG nanorod junction is much neater (extent ~1 μm) than the Au@PEG/CNT@PVA one (~10 μm). It stems from the nature of the first material of the junction: for Ag@SiO$_2$, evaporation still proceeds above the packed bed (*i.e.*, the activity is not reduced by the presence of colloids) which drains water but not colloids into the packed bed and forces a condition of *nonvanishing flux of water* at the level of the edge of the first material; newly coming particles of the second type will be dragged by the flow toward the interstices of the first material,[64,65] which blocks them and the second material builds up; as such, it represents an interesting option for studying the controlled hepitaxial growth of colloidal heterostructures. On the contrary, when evaporation stops in the first material (as for Au@PEG nanorods due to the presence of the polymer), the interface of the junction is smooth and the boundary condition is of *no flux*. Therefore, a composition gradient may occur on a spatial extend of order of $p \sim (D\tau_e)^{1/2}$, with D the diffusion coefficient of the colloids, which gives here $p \sim 10\ \mu$m for 50 nm colloids and $\tau_e = 50$ s.

Eventually, we also evidence here a way to grow dispersion for which the stability chart suggests it would not be possible directly in the microevaporator, for instance, because the ratio of colloids over traces of destabilizing agent is not favorable (Figure 3). This is the case of engineered raspberry-like nanoclusters (SiO_2@Ag@SiO_2, Figure 7c) which consist of a 86 nm silica core with 30 nm cubes grafted on the periphery and coated with a thin silica shell (≈5 nm). These clusters are meant to exhibit a specific plasmonic behavior[66] and their assemblies to possess exciting optical features. However, due to the high constraints required for their synthesis, their volume fraction is small, $\mathcal{O}(10^{-6})$, and they do not fulfill the growth condition of stability chart (Figure 3). To bypass this limitation, we construct a heterostructure based first on a millimeter-long colloidal crystal of 200 nm diameter polystyrene beads (tagged with fluorescein; see Figure 7c, top left) which acts as a packed bed; upon injection of the nanoraspberries, a dense state of the latter can be grown because the packed bed (pore size ≈10 nm) is permeable to water but not to NPs. Water along with traces of salt can flow inside the colloidal filter which retains the NPs, forcing them to pack and grow at a constant salinity, unlike the case of simple microevaporation which leads here to precipitation as both salt and NPs get concentrated. The resulting heterostructure can be extracted and observed with SEM, which effectively reveals that after the junction (size ∼μm) with the colloidal filter, the nanoraspberries form a tightly packed state with extended dimensions and an overall shape that reflects that of the microfluidic channel. In particular, the relatively flat faces of the material are quite appealing for the optical characterization (such as microellipsometry) we intend to carry on these 3D samples.

CONCLUSION

Evaporation has become a standard route for the guided assembly of nano- to microparticles. Here, we demonstrated that evaporation within dedicated microfluidic devices permits us to grow and shape-up solids made of NPs. As the microfluidic tool gives both a fine control over the kinetics of concentration and an easy observation in a model geometry, we could rationalize in which conditions the suspensions of NPs are likely to be turned into a solid by solvent extraction. The first criterion holds on the colloidal stability of the dilute suspension: we need to prevent precipitation before growth by carefully checking the amount of precipitant present in the initial stock solution. There is then virtually no limit to the growth and shape-up of all sorts of micromaterials made of NPs, as illustrated here for unary and binary spherical NPs, nanorods, *etc.* While we evidenced the presence of SLs, the coherence length of the latter remains small (∼μm) probably due either to a too-high polydispersity of the NPs or to the rate at which the solid is grown (which may overcome the natural rate of crystal growth). This issue is quite promising in terms of crystallinity, especially because we can redesign the microevaporator in order to slow the growth rate of the solid. Indeed, by tuning the humidity outside the device and the thickness of the channel, we can slow by a factor 10^2-10^3 the concentration kinetics and, hopefully, tune the way the material grows.

We also evidenced that the growth rate has intrinsic limits and illustrated two main limiting cases—evaporation- or transport-limited growth—which ultimately couple the physical chemistry of the dispersion to the concentration process. In all cases, it is possible to tune in time the dispersion to be concentrated in order to build tailor solids: we constructed heterojunctions between different types of NPs and colloidal filters that can retain dispersions that would precipitate otherwise.

We believe that the good control and rationalization of the growth process, along with the top-down/bottom-up combination offered by microfluidic evaporation, is promising; it could be useful in terms of fundamental understanding of the growth condition of a solid made of NPs and could also be device-oriented by controlling the placement of lumps or arrays of NPs in order to create new and functional microscale materials.

MATERIALS AND METHODS

Dispersions of NPs. *Gold Spherical NPs.* Tetrachloroauric acid ($HAuCl_4 \cdot 3H_2O$), tetraethylorthosilicate (TEOS), and NH_4OH (29%) were purchased from Aldrich, and sodium citrate ($C_6H_5O_7Na_3 \cdot 2H_2O$) was from Sigma. Cetyltrimethylammonium bromide (CTAB) and *O*-[2-(3-mercaptopropionylamino)ethyl]-*O*′-methylpoly(ethylene glycol) (mPEG-SH, M_w 5000) were provided by Fluka. Pure-grade ethanol and Milli-Q-grade water were used in all preparations. Unless otherwise stated, all of the chemicals were used without further purification.

Citrate-stabilized Au nanospheres (15 nm) were synthesized as described elsewhere.[67] mPEG-SH functionalization was carried out by dropwise addition of 1 mL of an aqueous solution 1.4×10^{-4} M mPEG-SH to 10 mL of as-synthesized 15 nm spheres ([Au] = 5×10^{-4} M). The mixture was allowed to react for 30 min and was cleaned by two centrifugation−redispersion cycles with ethanol.

Gold Nanorods. PEG-coated Au nanorods (NRs) were synthesized in two steps by modifying reported procedures. Initially, CTAB-coated Au nanorods were synthesized by adapting the protocol reported by Jana.[68] Subsequently, CTAB surfactants bound to the surface of Au nanorods were completely replaced by 5 kg/mol PEG-SH units following the procedure reported by Thierry *et al.*[69] The PEG-functionalized nanorods were characterized using TEM and UV−visible spectroscopy before use in our experiments; for more details, see Supporting Information.

Raspberry-like NPs. L-Arginine (99%), cyclohexane (=99.7%), TEOS (99%), sodium hydrosulfide (NaHS), poly(vinylpyrrolidone) (PVP; M_w = 55 000 g/mol), *N*-[3-(trimethoxysilyl)propyl]ethylenediamine (EDPS; 97%), and silver nitrate ($AgNO_3$; 99.9%) were purchased from Sigma-Aldrich. Ethylene glycol (EG) and ammonium hydroxide solution (27−30 wt %) were obtained from J.T. Baker. Absolute ethanol was purchased from Scharlau. All reagents and solvents are used without further purification.[70]

The silica NPs were prepared using a seed-mediated method.[70] Initially, silica "preseeds" were obtained as follows: 345 mL of an aqueous solution containing 7.5 mM of L-arginine was introduced in a 500 mL rounded beaker; 22.5 mL of cyclohexane was added, and the mixture was heated at 60 °C. When the mixture reached 60 °C, 37.5 mL of TEOS was introduced. The stirring was maintained for 24 h. Then, the mixture was passed to a rotavapor at 50 °C under vacuum to eliminate the cyclohexane. The concentration in silica seeds was determined by dry extract. These seeds were then grown in hydroalcoholic medium containing ammonia and wherein the TEOS was slowly and continuously introduced. Typically, 50 mL of ethanol, 5 mL of ammonium hydroxide corresponding to $[NH_3]$ = 1 M, then 5 mL of silica seed aqueous suspension were mixed in a 150 mL round beaker. The concentration in silica beads was determined by dry extract. A volume of 765 μL of EDPS aqueous solution corresponding to an excess of 20 compared with the grafting density of EDPS was quickly added into the previous silica suspension under magnetic stirring. The reaction mixture was stirred overnight. Then the mixture was washed by centrifugation at 15 000*g* for 20 min. The supernatant containing ethanol and oligomers of silanes was removed, and the bottom containing the modified particles was redispersed in absolute ethanol by sonication. This washing step was repeated five times. After removal of the last supernatant, the bottom was redispersed in 100 mL of deionized water and the pH of the solution was adjusted to 5.

The Ag NPs were synthesized by using a previously reported method.[63] First, a solution of NaHS (30 mM) and a solution of PVP (30 mg/L) in EG were prepared separately. The two solutions were left to age for 4 h under stirring. A 60 mL sample of EG was then introduced in a rounded flask mounted with a reflux condenser and heated at 150 °C for 2.5 h under stirring. Two hours later, argon flow was introduced. After 30 min, 35 μL of the aged NaHS solution and 15 mL of the PVP solution were injected in the reaction medium. Then, 5 mL of a $AgNO_3$ solution (0.16 M) in EG was quickly introduced. The solution turned yellow immediately. After 7 min, the reaction was quenched by quickly cooling the reaction flask in an ice bath. Finally, the Ag NPs were washed by centrifugation at 40 000*g* for 2 h and redispersed in ethanol. This centrifugation cycle was repeated twice. The mass concentration of silver NPs was determined by ICP-OES.

Typically, 0.2 mL of a diluted suspension of silica beads was dropwise introduced into 1 mL of the Ag nanoparticle solution. The silica bead solution was diluted such that the ratio concentration $[SiO_2 \text{ beads}]/[Ag]$ was about 1/100. The mixture was stirred overnight. Then the solution was diluted in 30 mL of an aqueous PVP solution (0.5 g/L). After 2 h, the mixture was washed three times by centrifugation at 3000*g* for 20 min and redispersed in water. The resulting $SiO_2@Ag$ nanostructures were once again centrifuged at 3000*g* for 20 min and redispersed in ethanol. Typically, 60 μL of ammonia was added to 5 mL of the $SiO_2@Ag$ suspension. Under stirring, 100 μL of a TEOS solution diluted in ethanol (1 vol %) was slowly added with an automatic syringe pump. The addition rate was fixed at 0.5 mL/h. The reaction mixture was stirred for 12 h at ≈20 °C. Upon completion of the growth of the silica shell, the particles were washed twice by centrifugation with ethanol.

$Ag@SiO_2$ Core−Shell NPs. The previously synthesized Ag nanoparticles were coated with silica by using a previously reported method.[63] Typically 3.75 mL of the Ag nanoparticle dispersion was mixed under continuous magnetic stirring with a solution of deionized water and ammonia, at a volume ratio of 93.8/5/1.2 for absolute ethanol, water, and ammonia, respectively. Then, 70 μL of TEOS was added, and the reaction mixture was stirred for 12 h at 20 °C. Upon completion of the growth of silica shell, the particles were washed by centrifugation with ethanol and finally redispersed in water.

Microfluidic Evaporation Cell. All structures were created using standard soft photolithography techniques. A master template was made with a photocurable resist which was then molded in PDMS and cured at high temperature. This elastomeric core was peeled off the template and punched to create an opening for the reservoir, either a polyethylene tubing or simply a large opening of 4 mm diameter; the body of the chip was then sealed with a thin PDMS membrane of thickness $e \approx 1020$ mm, and either the gradient technique or plasma activation was used to firmly bind the two elements. We used microscope slides to cover specific areas of the membrane where we wanted to suppress permeation and thus define the length L_0.[48]

Conflict of Interest: The authors declare no competing financial interest.

Acknowledgment. We are grateful to P. Barois, A. Aradian, A. Veltri, M. Albani, A. Grigorenko, and P. Maestro for fruitful comments and permanent enthusiasm, and to P. Poulin for kindly providing us with dispersions of carbon nanotubes. This work has been done within Long-Term-Project SC2267 at ESRF (European Synchrotron Radiation Facility, Grenoble, France) and received fundings from the European Union's Seventh Framework Programme (FP7/2008) under Grant Agreement No. 228762 and from Région Aquitaine.

Supporting Information Available: Simplified model accouting for the competition between evaporation-induced concentration and precipitation kinetics. Details concerning the synthesis of gold nanorods. This material is available free of charge *via* the Internet at http://pubs.acs.org.

REFERENCES AND NOTES

1. Talapin, D. V.; Lee, J. S.; Kovalenko, M. V.; Shevchenko, E. V. Prospects of Colloidal Nanocrystals for Electronic and Optoelectronic Applications. *Chem. Rev.* **2010**, *110*, 389–458.
2. Guerrero-Martinez, A.; Grzelczak, M.; Liz-Marzan, L. M. Molecular Thinking for Nanoplasmonic Design. *ACS Nano* **2012**, *6*, 3655–3662.
3. Engheta, N.; Salandrino, A.; Alú, A. Circuit Elements at Optical Frequencies: Nanoinductors, Nanocapacitors, and Nanoresistors. *Phys. Rev. Lett.* **2005**, *95*, 095504.
4. Boneschanscher, M. P.; Evers, W. H.; Qi, W.; Meeldijk, J. D.; Dijkstra, M.; Vanmaekelbergh, D. Electron Tomography Resolves a Novel Crystal Structure in a Binary Nanocrystal Superlattice. *Nano Lett.* **2013**, *13*, 1312–1316.
5. Nie, Z.; Petukhova, A.; Kumacheva, E. Properties and Emerging Applications of Self-Assembled Structures Made from Inorganic Nanoparticles. *Nat. Nanotechnol.* **2010**, *5*, 15–25.
6. Vanmaekelbergh, D. Self-Assembly of Colloidal Nanocrystals as Route to Novel Classes of Nanostructured Materials. *Nano Today* **2011**, *6*, 419–437.
7. Majetich, S.; Wen, T.; Booth, R. Functional Magnetic Nanoparticle Assemblies: Formation, Collective Behavior, and Future Directions. *ACS Nano* **2011**, *5*, 6081–6084.

8. Bao, N.; Gupta, A. Self-Assembly of Superparamagnetic Nanoparticles. *J. Mater. Res.* **2011**, *26*, 111–121.
9. Labastide, J. A.; Baghgar, M.; Dujovne, I.; Yang, Y.; Dinsmore, A. D.; Sumpter, B. G.; Venkataraman, D.; Barnes, M. D. Polymer Nanoparticle Super Lattices for Organic Photovoltaic Applications. *J. Phys. Chem. Lett.* **2011**, *2*, 3085–3091.
10. Gong, J.; Li, G.; Tang, Z. Self-Assembly of Noble Metal Nanocrystals: Fabrication, Optical Property, and Application. *Nano Today* **2012**, *7*, 564–585.
11. Grzelczak, M.; Liz-Marzan, L. M. Colloidal Nanoplasmonics: From Building Blocks to Sensing Devices. *Langmuir* **2013**, *29*, 4652–4663.
12. Bishop, K. J.; Wilmer, C. E.; Soh, S.; Grzybowski, B. A. Nanoscale Forces and Their Uses in Self-Assembly. *Small* **2009**, *5*, 1600–1630.
13. Shevchenko, E. V.; Talapin, D. V.; Kotov, N. A.; O'Brien, S.; Murray, C. B. Structural Diversity in Binary Nanoparticle Superlattices. *Nature* **2006**, *439*, 55–59.
14. Kimura, K.; Pradeep, T. Functional Noble Metal Nanoparticle Superlattices Grown at Interfaces. *Phys. Chem. Chem. Phys.* **2011**, *13*, 19214–19225.
15. Jones, M. R.; Macfarlane, R. J.; Lee, B.; Zhang, J.; Young, K. L.; Senesi, A. J.; Mirkin, C. A. DNA-Nanoparticle Superlattices Formed from Anisotropic Building Blocks. *Nat. Mater.* **2010**, *9*, 913–917.
16. Wang, Y.; Dai, Q.; Wang, L.; Zou, B.; Cui, T.; Liu, B.; Yu, W. W.; Hu, M. Z.; Zou, G. Mutual Transformation between Random Nanoparticles and Their Superlattices: The Configuration of Capping Ligand Chains. *J. Phys. Chem. C* **2010**, *114*, 11425–11429.
17. Feng, W.; Sun, L. D.; Yan, C. H. Role of Surface Ligands in the Nanoparticle Assemblies: A Case Study of Regularly Shaped Colloidal Crystals Composed of Sodium Rare Earth Fluoride. *Langmuir* **2011**, *27*, 3343–3347.
18. Coppel, Y.; Spataro, G.; Colliere, V.; Chaudret, B.; Mingotaud, C.; Maisonnat, A.; Kahn, M. L. Self-Assembly of ZnO Nanoparticles—An NMR Spectroscopic Study. *Eur. J. Inorg. Chem.* **2012**, *2012*, 2691–2699.
19. Walker, D. A.; Browne, K. P.; Kowalczyk, B.; Grzybowski, B. A. Self-Assembly of Nano-Triangle Superlattices Facilitated by Repulsive Electrostatic Interactions. *Angew. Chem., Int. Ed.* **2010**, *49*, 6760–6763.
20. Young, K. L.; Jones, M. R.; Zhang, J.; Macfarlane, R. J.; Esquivel-Sirvent, R.; Nap, R. J.; Wu, J.; Schatz, G. C.; Lee, B.; Mirkin, C. A. Assembly of Reconfigurable One-Dimensional Colloidal Superlattices Due to a Synergy of Fundamental Nanoscale Forces. *Proc. Natl. Acad. Sci. U.S.A.* **2012**, *109*, 2240–2245.
21. Rupich, S. M.; Shevchenko, E. V.; Bodnarchuk, M. I.; Lee, B.; Talapin, D. V. Size-Dependent Multiple Twinning in Nanocrystal Superlattices. *J. Am. Chem. Soc.* **2010**, *132*, 289–296.
22. Goubet, N.; Richardi, J.; Albouy, P. A.; Pileni, M. P. Which Forces Control Supracrystal Nucleation in Organic Media? *Adv. Funct. Mater.* **2011**, *21*, 2693–2704.
23. Kalsin, A. M.; Fialkowski, M.; Paszewski, M.; Smoukov, S. K.; Bishop, K. J. M.; Grzybowski, B. A. Electrostatic Self-Assembly of Binary Nanoparticle Crystals with a Diamond-like Lattice. *Science* **2006**, *312*, 420–424.
24. Talapin, D. V.; Shevchenko, E. V.; Bodnarchuk, M. I.; Ye, X.; Chen, J.; Murray, C. B. Quasicrystalline Order in Self-Assembled Binary Nanoparticle Superlattices. *Nature* **2009**, *461*, 964–967.
25. Cheng, W.; Campolongo, M. J.; Tan, S. J.; Luo, D. Free-standing Ultrathin Nano-Membranes *via* Self-Assembly. *Nano Today* **2009**, *4*, 482–493.
26. Henzie, J.; Grunwald, M.; Widmer-Cooper, A.; Geissler, P. L.; Yang, P. Self-Assembly of Uniform Polyhedral Silver Nanocrystals into Densest Packings and Exotic Superlattices. *Nat. Mater.* **2012**, *11*, 131–137.
27. Martin, A.; Schopf, C.; Pescaglini, A.; O'Riordan, A.; Iacopino, D. Synthesis, Optical Properties and Self-Assembly of Gold Nanorods. *J. Exp. Nanosci.* **2012**, *7*, 688–702.
28. Hanrath, T.; Choi, J. J.; Smilgies, D. M. Structure/Processing Relationships of Highly Ordered Lead Salt Nanocrystal Superlattices. *ACS Nano* **2009**, *3*, 2975–2988.
29. Huang, T.; Zhao, Q.; Xiao, J.; Qi, L. Controllable Self-Assembly of PbS Nanostars into Ordered Structures: Close-Packed Arrays and Patterned Arrays. *ACS Nano* **2010**, *4*, 4707–4716.
30. Grzelczak, M.; Vermant, J.; Furst, E. M.; Liz-Marzan, L. M. Directed Self-Assembly of Nanoparticles. *ACS Nano* **2010**, *4*, 3591–3605.
31. Deegan, R. D.; Bakajin, O.; Dupont, T. F.; Huber, G.; Nagel, S. R.; Witten, T. A. Capillary Flow as the Cause of Ring Stains from Dried Liquid Drops. *Nature* **1997**, *389*, 827–829.
32. Tekin, E.; Smith, P. J.; Schubert, U. S. Inkjet Printing as a Deposition and Patterning Tool for Polymers and Inorganic Particles. *Soft Matter* **2008**, *4*, 703–713.
33. Prevo, B. G.; Kuncicky, D. M.; Velev, O. D. Engineered Deposition of Coatings from Nano- and Micro-Particles: A Brief Review of Convective Assembly at High Volume Fraction. *Colloids Surf., A* **2007**, *311*, 2–10.
34. Kumnorkaew, P.; Ee, Y. K.; Tansu, N.; Gilchrist, J. F. Investigation of the Deposition of Microsphere Monolayers for Fabrication of Microlens Arrays. *Langmuir* **2008**, *24*, 12150–12157.
35. Yang, S. M.; Miguez, H.; Ozin, G. A. Opal Circuits of Light Planarized Microphotonic Crystal Chips. *Adv. Funct. Mater.* **2002**, *12*, 425–431.
36. Podsiadlo, P.; Krylova, G. V.; Demortiere, A.; Shevchenko, E. V. Multicomponent Periodic Nanoparticle Superlattices. *J. Nanopart. Res.* **2011**, *13*, 15–32.
37. Curri, M. L.; Comparelli, R.; Striccoli, M.; Agostiano, A. Emerging Methods for Fabricating Functional Structures by Patterning and Assembling Engineered Nanocrystals. *Phys. Chem. Chem. Phys.* **2010**, *12*, 11197–11207.
38. Taheri, S. M.; Fischer, S.; Trebbin, M.; With, S.; Schroeder, J. H.; Perlich, J.; Roth, S. V.; Foerster, S. Lyotropic Phase Behavior of Polymer-Coated Iron Oxide Nanoparticles. *Soft Matter* **2012**, *8*, 12124–12131.
39. Bodnarchuk, M. I.; Li, L.; Fok, A.; Nachtergaele, S.; Ismagilov, R. F.; Talapin, D. V. Three-Dimensional Nanocrystal Superlattices Grown in Nanoliter Microfluidic Plugs. *J. Am. Chem. Soc.* **2011**, *133*, 8956–8960.
40. Akey, A.; Lu, C.; Yang, L.; Herman, I. Formation of Thick, Large-Area Nanoparticle Superlattices in Lithographically Defined Geometries. *Nano Lett.* **2010**, *10*, 1517–1521.
41. Chattopadhyay, S.; Mukherjee, R.; Datta, A.; Saha, A.; Sharma, A.; Kulkarni, G. U. Self-Assembly of a Two-Dimensional Au-Nanocluster Superlattice and Its Photoluminescence Spectra. *J. Nanosci. Nanotechnol.* **2009**, *9*, 190–194.
42. Cheng, W.; Campolongo, M. J.; Cha, J. J.; Tan, S. J.; Umbach, C. C.; Muller, D. A.; Luo, D. Free-Standing Nanoparticle Superlattice Sheets Controlled by DNA. *Nat. Mater.* **2009**, *8*, 519–525.
43. Chen, Y.; Fu, J.; Ng, K. C.; Tang, Y.; Cheng, W. Free-Standing Polymer-Nanoparticle Superlattice Sheets Self-Assembled at the Air Liquid Interface. *Cryst. Growth Des.* **2011**, *11*, 4742–4746.
44. Leng, J.; Lonetti, B.; Tabeling, P.; Joanicot, M.; Ajdari, A. Microevaporators for Kinetic Exploration of Phase Diagrams. *Phys. Rev. Lett.* **2006**, *96*, 084503.
45. Leng, J.; Salmon, J.-B. Microfluidic Crystallization. *Lab Chip* **2009**, *9*, 24–34.
46. Salmon, J.-B.; Leng, J. Detailed Functioning of Microevaporators and of Their Application to the Dynamic Exploration of Phase Diagram. *J. Appl. Phys.* **2010**, 084905.
47. Merlin, A.; Angly, J.; Daubersies, L.; Madeira, C.; Schoeder, S.; Leng, J.; Salmon, J.-B. Time-Resolved Microfocused Small-Angle X-ray Scattering Investigation of the Microfluidic Concentration of Charged Nanoparticles. *Eur. Phys. J. E* **2011**, *34*, 58.
48. Merlin, A.; Salmon, J.-B.; Leng, J. Microfluidic-Assisted Growth of Colloidal Crystals. *Soft Matter* **2012**, *8*, 3526–3537.
49. Daubersies, L.; Leng, J.; Salmon, J.-B. Steady and Out-of-Equilibrium Phase Diagram of a Complex Fluid at the Nanoliter Scale: Combining Microevaporation, Confocal Raman Imaging and Small Angle X-ray Scattering. *Lab Chip* **2012**, *13*, 910–919.

50. Kim, E.; Xia, Y. N.; Whitesides, G. M. Two- and Three-Dimensional Crystallization of Polymeric Microspheres by Micromolding in Capillaries. *Adv. Mater.* **1996**, *8*, 245.
51. Shiu, J. Y.; Kuo, C. W.; Chen, P. Actively Controlled Self-Assembly of Colloidal Crystals in Microfluidic Networks by Electrocapillary Forces. *J. Am. Chem. Soc.* **2004**, *126*, 8096–8097.
52. Schindler, M.; Ajdari, A. Modeling Phase Behavior for Quantifying Micro-Pervaporation Experiments. *Eur. Phys. J. E* **2009**, *28*, 27–45.
53. Noblin, X.; Mahadevan, L.; Coomaraswamy, I. A.; Weitz, D. A.; Holbrook, N. M.; Zwieniecki, M. A. Optimal Vein Density in Artificial and Real Leaves. *Proc. Natl. Acad. Sci. U.S.A.* **2008**, 9140–9144.
54. Wheeler, T. D.; Stroock, A. D. The Transpiration of Water at Negative Pressures in a Synthetic Tree. *Nature* **2008**, *455*, 208–212.
55. Russel, W. B.; Saville, D. A.; Schowalter, W. R. *Colloidal Dispersions*; Cambridge University Press: Cambridge, UK, 1992.
56. Sirota, E. B.; Ou-Yang, H. D.; Sinha, S. K.; Chaikin, P. M.; Axe, J. D.; Fujii, Y. Complete Phase Diagram of a Charged Colloidal System: A Synchrotron X-ray Scattering Study. *Phys. Rev. Lett.* **1989**, *62*, 1524.
57. Forster, S.; Timmann, A.; Konrad, M.; Schellbach, C.; Meyer, A.; Funari, S. S.; Mulvaney, P.; Knott, R. Scattering Curves of Ordered Mesoscopic Materials. *J. Phys. Chem. B* **2005**, *109*, 1347–1360.
58. Forster, S.; Timmann, A.; Schellbach, C.; Fromsdorf, A.; Kornowski, A.; Weller, H.; Roth, S. V.; Lindner, P. Order Causes Secondary Bragg Peaks in Soft Materials. *Nat. Mater.* **2007**, *6*, 888–893.
59. Davis, K. E.; Russel, W. B.; Glantschnig, W. J. Settling Suspensions of Colloidal Silica: Observations and X-ray Measurements. *J. Chem. Soc., Faraday Trans.* **1991**, *87*, 411–424.
60. Hung, A. M.; Konopliv, N. A.; Cha, J. N. Solvent-Based Assembly of CdSe Nanorods in Solution. *Langmuir* **2011**, 12322–12328.
61. Xie, Y.; Guo, S.; Ji, Y.; Guo, C.; Liu, X.; Chen, Z.; Wu, X.; Liu, Q. Self-Assembly of Gold Nanorods into Symmetric Superlattices Directed by OH-Terminated Hexa(ethylene glycol) Alkanethiol. *Langmuir* **2011**, 11394–11400.
62. Hamon, C.; Postic, M.; Mazari, E.; Bizien, T.; Dupuis, C.; Even-Hernandez, P.; Jimenez, A.; Courbin, L.; Gosse, C.; Artzner, F.; *et al.* Three-Dimensional Self-Assembling of Gold Nanorods with Controlled Macroscopic Shape and Local Smectic B Order. *ACS Nano* **2012**, *6*, 4137–4146.
63. Massé, P.; Mornet, S.; Duguet, E.; Tréguer-Delapierre, M.; Ravaine, S.; Iazzolino, A.; Salmon, J.-B.; Leng, J. Synthesis of Size-Monodisperse Spherical Ag@SiO$_2$ Nanoparticles and 3D Assembly Assisted by Microfluidics. *Langmuir* **2013**, *29*, 1790–1795.
64. Brewer, D. D.; Allen, J.; Miller, M. R.; de Santos, J. M.; Kumar, S.; Norris, D. J.; Tsapatsis, M.; Scriven, L. E. Mechanistic Principles of Colloidal Crystal Growth by Evaporation-Induced Convective Steering. *Langmuir* **2008**, *24*, 13683–13693.
65. Gasperino, D.; Meng, L.; Norris, D. J.; Derby, J. J. The Role of Fluid Flow and Convective Steering during the Assembly of Colloidal Crystals. *J. Cryst. Growth* **2008**, *310*, 131–139.
66. Muehlig, S.; Cunningham, A.; Scheeler, S.; Pacholski, C.; Buergi, T.; Rockstuhl, C.; Lederer, F. Self-Assembled Plasmonic Core−Shell Clusters with an Isotropic Magnetic Dipole Response in the Visible Range. *ACS Nano* **2011**, *5*, 6586–6592.
67. Enustun, B.; Turkevich, J. Coagulation of Colloidal Gold. *J. Am. Chem. Soc.* **1963**, *85*, 3317.
68. Jana, N. Gram-Scale Synthesis of Soluble, Near-Monodisperse Gold Nanorods and Other Anisotropic Nanoparticles. *Small* **2005**, *1*, 875–882.
69. Thierry, B.; Ng, J.; Krieg, T.; Griesser, H. A Robust Procedure for the Functionalization of Gold Nanorods and Noble Metal Nanoparticles. *Chem. Commun.* **2009**, 1724–1726.
70. Désert, A.; Chaduc, I.; Fouilloux, S.; Taveau, J.-C.; Lambert, O.; Lansalot, M.; Bourgeat-Lami, E.; Thill, A.; Spalla, O.; Ravaine, S.; *et al.* High-Yield Preparation of Polystyrene/Silica Clusters of Controlled Morphology. *Polym. Chem.* **2012**, *3*, 1130–1132.